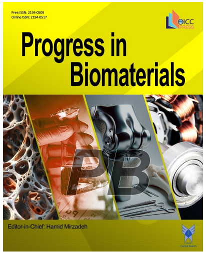

Prog. Biomater. 2026; 15(1) : 1-15

Progress in Biomaterials (PIBM)

https://doi.org/10.57647/pibm.2026.152601

Research Article

From Inscription Threshold to Realistic Spectral Response in Type I Fiber Bragg Gratings for Biomedical Sensing

Ali Kamal Nooshabadi, Fazel Jahangiri*

Laser Plasma Research Institute, Shahid Beheshti University, Tehran, Iran

*Corresponding author: f_jahangiri@sbu.ac.ir

Article History

Received:
19 December 2025

Revised:
22 January 2026

Accepted:
8 March 2026

Published in Issue:
31 March 2026

Abstract:

Despite the high potential of type I fiber Bragg gratings (FBGs), with narrow spectral features and high stability for non-invasive biosensing, several challenges still limit their performance. Reliable theoretical criteria for determining the laser parameters required to inscribe type I FBGs without damage remain limited. Moreover, conventional models often fail to accurately predict the spectral response of inscribed FBGs, especially in the presence of cladding-mode coupling and realistic transverse refractive-index modulation (RIM) profiles. In this work, the temporal evolution of free-electron density and total induced absorption under femtosecond-pulse irradiation are calculated and linked to an experimental metric based on optical transmission reduction. Using this approach, the type I inscription threshold is determined. The obtained results show that the onset of type I inscription occurs at a peak intensity 1.3107×10^{13} W/cm^2 (2.092 J/cm^2). Furthermore, a full-wave three-dimensional electromagnetic model based on the finite element method is developed for type I FBGs with core–cladding mode coupling and realistic transverse RIM profiles. The developed model further reveals that the coupling behavior and transverse RIM profile provide effective control over the depth and wavelength of the main Bragg resonance, as well as the position and intensity of shorter-wavelength side resonances. These findings provide a basis for realistic FBG spectral engineering and optimized biosensor design.

Keywords: FBG; Type I FBG; Inscription threshold; Cladding mode coupling; Finite element method; Biosensing

Cite this article: Nooshabadi AK, Jahangiri F. From Inscription Threshold to Realistic Spectral Response in Type I Fiber Bragg Gratings for Biomedical Sensing. Prog. Biomater. 2026;15(1), 1-15. https://doi.org/10.57647/pibm.2026.152601

1. Introduction

Fiber Bragg gratings (FBGs), as optical fiber-based sensing elements, have attracted increasing attention over the past few decades due to their wide applicability in biosensing and non-invasive vital-sign monitoring. Their relevance arises mainly from their ability to detect small and repeatable strain variations, enabling accurate recording of vascular pulse waveforms and extraction of hemodynamic indices. Therefore, these sensors can support the non-invasive estimation of blood pressure and heart rate in wearable systems [1, 2].

In addition, the inherent properties of optical fibers, including immunity to electromagnetic interference, biocompatibility, small size, lightweight structure, and multiplexing capability, enable their safe integration into medical devices and systems. These features also facilitate reliable operation in environments where electronic sensors face serious limitations, such as near MRI systems or in areas with strong electromagnetic noise. Moreover, in molecular biosensing, surface functionalization of FBGs allows specific biological interactions, such as antigen–antibody binding or DNA hybridization, to be converted into detectable and quantifiable optical changes. This provides a platform for developing FBG-based biosensors for diagnostic applications [3, 4, 5, 6].

Despite the significant potential of FBGs, not all grating types are equally suitable for biosensing applications.

The performance of these systems depends strongly on the grating type and its intrinsic properties, including the stability and controllability of the spectral response, as well as long-term mechanical and functional durability. These characteristics are largely governed by the quality and method of FBG fabrication; therefore, careful selection and optimization of the fabrication process play a decisive role in the practical implementation of FBG-based biomedical and clinical applications.

Among different fabrication methods, inscription using femtosecond infrared (fs-IR) lasers has emerged as a leading approach to address this need [7, 8, 9]. These lasers induce localized nonlinear absorption in the fiber core through ultrashort, high-intensity pulses, enabling controlled inscription of FBGs without removing the fiber cladding in a wide range of optical fibers. Depending on the refractive-index modulation (RIM) induced by the interaction between fs-IR laser pulses and the fiber, FBGs are commonly classified into type I and type II gratings. Type I FBGs are formed through non-damaging processes, such as glass densification and color-center formation, whereas type II FBGs result from damage-related mechanisms, such as nanograting or micro-explosion formation [10, 11].

The main characteristic of type I FBGs is a smooth and isotropic RIM, typically in the range of $\Delta n \approx 10^{-4}$ to $\Delta n \approx 10^{-3}$; which results in a clean spectral response with low scattering losses. In addition, the high mechanical strength and long fatigue lifetime of type I FBGs make them suitable for long-term applications, especially in fiber lasers and optical sensors operating in moderate-temperature environments [10, 11]. In contrast, type II FBGs are characterized by an anisotropic RIM, typically on the order of $\Delta n \approx 10^{-2}$, which can increase scattering losses and reduce mechanical strength. Consequently, their long-term stability and reliability may be lower than those of type I FBGs in applications where mechanical durability and low-loss spectral performance are required [10, 11]. Accordingly, the present study focuses on the interaction physics and optical modeling of type I FBGs inscribed using an fs-IR laser.

Despite the significant advantages of type I FBGs, achieving their optimal performance faces two major challenges for which no theoretical framework or accurate simulation model has yet been presented. The first challenge is determining and controlling the optimal fs-IR laser fluence and intensity required to induce isotropic RIM in the fiber core, which is a highly sensitive issue given the narrow window between the type I and type II regimes. The second challenge, which remains even with precise control of the laser fluence and intensity, is related to the spatial distribution of RIM across the core cross-section, which directly affects the spectral response of FBGs, particularly their reflection and optical loss characteristics.

Regarding the first challenge, the damage threshold of silica glass under fs-IR laser irradiation has been previously described using models based on critical free-electron [12, 13]. However, no theoretical framework has been established to identify the initiation threshold of isotropic RIM during type I FBG inscription or to clarify the mechanisms governing it. Existing reports only indicate that this RIM occurs at an intensity lower than the fiber damage threshold [11], while the exact boundaries among the three regimes—no RIM, isotropic RIM, and damage initiation—remain unclear. In the absence of such a model, determining the optimal fs-IR irradiation conditions for type I FBG inscription mainly relies on experimental trial and error, which limits controllability, reproducibility, and scalability. Therefore, developing a physical model capable of predicting the fs-IR laser fluence and intensity thresholds for the initiation of isotropic RIM remains an unmet need in type I FBG fabrication.

In addition to determining the intensity and fluence thresholds, the second challenge concerns the transverse RIM profile in the fiber core, which plays a crucial role in shaping the spectral response of FBGs and therefore cannot be neglected in grating design [14, 15]. In FBGs directly inscribed using fs-IR lasers, this profile is rarely ideal, i.e., homogeneous and extending over the entire core. In particular, point-by-point writing typically produces localized and asymmetric RIM profiles, whereas more recent plane-by-plane techniques can generate more symmetric profiles, although they often do not cover the entire core cross-section [7, 9].

Non-ideal RIM profiles can break the cylindrical symmetry of the core, enhance mode coupling, and transfer part of the optical power from the fundamental core mode to cladding modes [14, 15]. However, conventional analytical models based on coupled-mode theory often assume an ideal and uniform RIM profile and therefore neglect core–cladding coupling. As a result, these models mainly describe the coupling of the forward-propagating fundamental core mode to its reflected counterpart, while they may fail to reproduce the full spectral response, particularly the side resonances caused by core–cladding coupling in type I FBGs directly inscribed using fs-IR lasers [16, 17, 18]. Such side resonances, appearing at wavelengths shorter than the main Bragg resonance, have been clearly reported in many experimental studies [19, 14, 20] In some cases, however, the reported theoretical results failed to reproduce these resonances despite their experimental observation [20].

This issue is particularly important in biosensing applications. In such applications, cladding modes are highly sensitive to changes in the medium surrounding the fiber, including variations in the external refractive index, the presence of functional coatings, surface functionalization, and biomolecular binding events [3, 4, 6]. Therefore, spectral changes induced by core–cladding coupling, especially the characteristics of side resonances, can carry valuable sensing information. Accordingly, any analytical or design framework aimed at accurately describing the behavior of FBGs in biological environments should quantitatively and realistically account for the transverse RIM profile and its effects on coupling coefficients and spectral response, rather than neglecting or oversimpli-

https://doi.org/10.57647/pibm.2026.152601

fying these effects by assuming a uniform RIM over the entire core cross-section.

In recent years, several efforts have been made to develop more advanced theoretical models, particularly for analyzing the spectral response of type II FBGs. These models, based on full-vectorial coupled-mode theory and three-layer circular fiber structures, have reconstructed the spectral response of type II FBGs with inhomogeneous and asymmetric RIMs using analytical approaches such as Fourier expansion and the virtual cutoff concept [21, 22]. In these approaches, the coupling coefficients are calculated through overlap integrals of the electromagnetic fields. Under the synchronous approximation, these models provide a physically meaningful description of core–cladding coupling and side resonances. Nevertheless, their dependence on geometric approximations and their primary focus on type II FBGs limit their direct applicability to type I FBGs. This limitation highlights the need for more accurate quantitative models to predict the spectral response of type I FBGs inscribed using fs-IR lasers.

This study addresses the key challenges associated with type I FBGs directly inscribed using fs-IR lasers through a two-step complementary approach. In the first step, a physical model is developed to determine the threshold fs-IR laser fluence and peak intensity required to induce isotropic RIM in the fiber core. By combining theoretical analysis with experimental data, the model defines the boundaries among three key regimes—no RIM, isotropic RIM formation, and damage initiation—while also clarifying the nonlinear processes responsible for the formation of type I RIM.

In the second step, a full-wave electromagnetic model based on the finite element method (FEM) is developed to predict the spectral response of type I FBGs. By solving the Helmholtz wave equation in the three-dimensional grating structure, the model enables detailed analysis of the electromagnetic-field distribution and the effects of core–cladding mode coupling and transverse RIM profiles on the spectral properties of the grating.

Overall, addressing these two challenges enables more realistic and controllable prediction of the spectral response of type I FBGs, bringing the model closer to experimental behavior. This can improve the reliability and accuracy of FBG-based sensing systems in biomedical applications.

The obtained results indicate that the fs-IR laser fluence threshold required for type I FBG inscription is lower than the structural damage threshold of the fiber. At the inscription threshold, the free-electron density remains below the critical value, with multiphoton photoionization acting as the dominant mechanism for initiating isotropic RIM, while avalanche ionization plays a secondary role. Ultimately, the proposed framework quantitatively defines the transition boundaries among the three key regimes of the inscription process and enables precise control of laser irradiation conditions without reliance on trial-and-error approaches.

Urthermore, the spectral modeling results reveal that the transverse RIM profile can be engineered to control the reflectivity and wavelength of the main Bragg resonance and, through core–cladding mode coupling, to tune the position and intensity of shorter-wavelength side resonances. Such effects are often neglected in previous studies, although they are important for designing and optimizing the performance of type I FBGs. This integrated framework connects fundamental inscription challenges to practical spectral-engineering solutions and provides a basis for further advances in type I FBG-based sensing systems.

The structure of this paper is organized as follows. Section 2 introduces the theoretical model of femtosecond-laser interaction with optical fiber, focusing on nonlinear absorption mechanisms and the criterion for determining the type I inscription threshold. Section 3 describes the FEM-based optical model and the simulation of FBG spectral responses using realistic transverse RIM profiles. Section 4 analyzes the results of the two models and presents the key findings of the study.

2. Theoretical framework for determining the inscription threshold of type-I FBG

The interaction of an fs-IR laser pulse with silica glass is a highly nonlinear process whose behavior strongly depends on the pulse peak intensity. At low intensities, silica remains nearly transparent and no significant optical modification is observed. However, when the peak intensity approaches the order of 10^{13} W/cm^2, nonlinear absorption is initiated through photoionization. In this process, valence-band electrons acquire sufficient energy to cross the bandgap of silica under the strong laser electric field, either through the simultaneous absorption of multiple photons, i.e., multiphoton ionization, or through quantum tunneling across a field-distorted potential barrier. The relative contribution of each mechanism depends on the laser intensity. As a result, seed free electrons are generated in the conduction band, and their density can subsequently increase through avalanche ionization. The increase in free-electron density enhances absorption and reduces the optical transmittance (T), which can ultimately lead to localized RIM formation in the silica structure [12].

Previous experimental observations indicate that the first localized RIM induced in silica glass by fs-IR laser irradiation is isotropic and smooth. This transition begins when the transmittance of the sample decreases from an initial value of approximately 100% to about 94%. This small but measurable reduction is used as an experimental threshold for the transition from the transparent regime to the isotropic RIM regime [23, 24]. With further increases in laser fluence and peak intensity beyond this threshold, the RIM gradually evolves from an isotropic modification toward anisotropic structures and eventually enters the damage-related type II regime.

To quantitatively describe this experimental behavior, we use the optical transmission relation $T = \exp(-\alpha_{tot} L)$ where α_{tot} is the total absorption coefficient of the material, including both linear and nonlinear absorption mechanisms, and (L) is the effective interaction length. During type I FBG inscription using an fs-IR laser, the beam is directly focused into the fiber core; therefore, nonlinear absorption and RIM formation occur predominantly within the focal volume of the core. Accordingly (L) is approximated by the fiber core diameter. By substituting $T = 0.94$ and $L = 8.2$ µm into the transmission equation, the total absorption coefficient corresponding to the experimental threshold is obtained as $\alpha_{tot,exp} \approx 7.37 \times 10^3$ m^{-1}. This value is used as the experimental reference for the modeling in this study.

The next objective is to calculate the temporal evolution of the total absorption coefficient α_{tot} during fs-IR pulse irradiation and determine the fluence and peak intensity at which α_{tot} reaches $\alpha_{tot,exp}$ at the end of the interaction. These values define the threshold conditions for the onset of isotropic RIM and, consequently, for type I FBG inscription. For this purpose, the temporal evolution of α_{tot} during pulse interaction is modeled using the following relation [25]:

$$\alpha_{tot}(t) = \frac{4\pi\kappa(t)}{\lambda} = \frac{4\pi}{\lambda}\left\{\frac{1}{2}\left[(\varepsilon_1^2(t) + \varepsilon_2^2(t))^{\frac{1}{2}} - \varepsilon_1(t)\right]\right\}^{\frac{1}{2}} \quad (1)$$

In this relation, the extinction coefficient κ is directly related to the real components $\varepsilon_1(t)$ and imaginary $\varepsilon_2(t)$ of the complex dielectric function of the material. These two components represent the scattering of light and the absorption of laser energy in the material, respectively, and are directly related to the dynamics of the free electron density $n(t)$ according to the Drude model [26]:

$$\varepsilon_1(t) = \varepsilon_{opt} - \frac{n(t)e^2}{\varepsilon_0 m_e^*} \times \frac{1}{\omega^2 + \frac{1}{\tau_D^2}} \quad (2)$$

$$\varepsilon_2(t) = \frac{n(t)e^2\tau_D}{\varepsilon_0 m_e^* \omega(1 + \omega^2\tau_D^2)} \quad (3)$$

where $\varepsilon_{opt} = n_0^2$ is the dielectric constant of the unexcited material, n_0 is the refractive index of the material, ε_0 is the permittivity of free space, m_e^* is the effective mass of an electron, e is the electron charge, ω is the angular frequency of the laser, and τ_D is the Drude relaxation time.

According to this formulation, the calculation of α_{tot} requires the determination of two components $\varepsilon_1(t)$ and $\varepsilon_2(t)$, which themselves are functions of $n(t)$. Therefore, the key step in this analysis is to model the time dynamics of $n(t)$ by solving the following rate equation [13, 27, 28, 26]:

$$\frac{\partial n(t)}{\partial t} = W_{PI}(I(t)) + W_{AV}(I(t)) \cdot n(t) - W_R(n(t), t) \quad (4)$$

where W_{PI} and W_{AV} represent the rates of increase in the free-electron density due to photoionization and avalanche ionization processes, respectively, and W_R represents the relaxation rate from the conduction band to other electronic states. The excitation rates can be described based on the Keldysh theory for photoionization and the Drude model for free carrier absorption. In this framework, the expression for the photoionization rate W_{PI} (equation (4)), which includes various material parameters as well as Dawson and elliptic integrals, is given by [29]:

$$W_{PI}(I(t)) = \frac{2\omega}{9\pi}\left(\frac{\omega m_r^*}{\hbar\sqrt{\gamma_1}}\right)^{\frac{3}{2}} \times Q(\gamma, x) \times \exp\left\{-\pi\langle x+1\rangle \frac{K(\gamma_1) - E(\gamma_1)}{E(\gamma_2)}\right\} \quad (5)$$

where the function $Q(\gamma, x)$ is defined as follows:

$$Q(\gamma, x) = \sqrt{\frac{\pi}{2K(\gamma_2)}} \times \sum_{n=0}^{\infty} \exp\left\{-n\pi \frac{K(\gamma_2) - E(\gamma_2)}{E(\gamma_1)}\right\} \times \Phi\left\{\frac{\pi}{2}\sqrt{\frac{(2\langle x+1\rangle - 2x + n)}{K(\gamma_2)E(\gamma_2)}}\right\} \quad (6)$$

In the above equation, Φ denotes the Dawson function, and E and K are the complete elliptic integrals of the first and second kinds, respectively. To simplify the expressions in terms of the Keldysh parameter γ, two variables $\gamma_1 = \frac{\gamma^2}{1+\gamma^2}$ and $\gamma_2 = \frac{1}{1+\gamma^2}$ are defined. The quantity $\langle x+1\rangle$ also represents the minimum number of photons with frequency ω required to cross the energy band gap and is given by the following expression [27]:

$$x = \frac{2}{\pi}\frac{E_g}{\hbar\omega}\frac{\sqrt{1+\gamma^2}}{\gamma}E\frac{1}{1+\gamma^2} \quad (7)$$

where E_g is the intrinsic bandgap energy of the material.

For a clearer physical interpretation, the photoionization rate can be analyzed in terms of the Keldysh parameter. The Keldysh parameter is defined as $\gamma = \omega\sqrt{E_g m_r^*}/eE$, where E is the electric-field amplitude of the laser radiation anddenotes the reduced mass of the electron and m_r^* is the reduced effective mass of the electron–hole pair, given by $m_r^* = m_e m_h/m_e + m_h$. Based on the value of γ, the ionization process can be divided into two limiting regimes: The multiphoton ionization regime and the tunneling ionization regime. In the high-frequency and low-electric-field limit ($\gamma \gg 1$), photoionization is dominated by multiphoton ionization (MPI), and the corresponding ionization rate can be approximated as follows [13, 26, 27, 28]:

$$W_{\text{MPI}} = \frac{2\omega}{9\pi}\left(\frac{\omega m_r^*}{\hbar}\right)^{\frac{3}{2}} \times \Phi\left(\sqrt{2\left\langle\frac{E_g}{\hbar\omega}+1\right\rangle - 2\frac{E_g}{\hbar\omega}}\right) \times \exp\left\{2\left\langle\frac{E_g}{\hbar\omega}+1\right\rangle\left(1 - \frac{1}{4\gamma^2}\right)\right\}\left(\frac{1}{16\gamma^2}\right)^{\left\langle\frac{E_g}{\hbar\omega}+1\right\rangle} \quad (8)$$

where $\widetilde{E_g} = E_g[1 + (1/2\gamma^2)]$ represents the effective bandgap energy in the radiation field. In the high-electric-field and low-frequency limit ($\gamma \ll 1$), photoionization is governed by tunneling ionization (TI), and the ionization

https://doi.org/10.57647/pibm.2026.152601

rate can be approximated as follows:

$$W_{\mathrm{TI}} = \frac{2\omega}{9\pi^2\hbar}\left(\frac{m_r^* E_g}{\hbar^2}\right)^{\frac{3}{2}}\left(\frac{h\omega}{E_g\gamma}\right)^{\frac{5}{2}} \exp\left\{-\frac{\pi}{2}\frac{E_g\gamma}{\hbar\omega}\left(1-\frac{\gamma^2}{8}\right)\right\} \quad (9)$$

To select an appropriate approximation for the photoionization rate, the total photoionization rate was plotted together with the MPI and TI rates using the parameters listed in Table 1 (the corresponding plot is provided in the Supplementary Information). As shown in this comparison, for peak intensities below 10^{14} W/cm^2, the total photoionization rate obtained from the full Keldysh formulation closely follows the MPI-limit rate. Since the type I FBG inscription conditions considered in this work lie within this intensity range ($I < 10^{14}$ W/cm^2), the model is simplified, without significant loss of accuracy, by calculating W_{PI} using the MPI-limit expression, i.e., Eq. (8), instead of the full Keldysh expression in Eq. (5).

The second major contribution to the ionization process can be attributed to avalanche ionization. This phenomenon is a cascade process in which free electrons in the conduction band, by absorbing energy from the laser field, reach the energy level necessary to excite valence band electrons and transfer them to the conduction band. The avalanche ionization rate can be calculated using the Drude model, which assumes that the heating of conduction electrons due to photon absorption behaves similarly to free electrons in metals. According to this model, the W_{AV} rate is expressed as follows [30]:

$$W_{AV}(I(t)) = \frac{\sigma}{E_g} I(t) \quad (10)$$

In this relation, σ is the absorption cross section of energy by a free electron, which itself depends on the properties of the material and the plasma:

$$\sigma = \frac{e^2}{c\varepsilon_0 n_0 m_e^*} \times \frac{\tau_c}{1+\omega^2\tau_c^2} \quad (11)$$

Additionally, τ_c is the mean collision time between electrons, which is inversely proportional to the free-carrier density and is defined as follows:

$$\tau_c = \frac{16\pi\varepsilon_0^2\sqrt{m_e^*(0.1E_g)^3}}{\sqrt{2}e^4 n(t)} \quad (12)$$

To complete the rate-model description, the relaxation process represented by W_R in Eq. (4) must also be considered. In germanium-doped silica glass, which forms the core material of many commercial optical fibers, including the SMF-28 fiber used in this experiment, a major relaxation pathway for the free-electron population on the femtosecond timescale is the formation of self-trapped excitons. This ultrafast process involves the rapid localization of excited carriers in the germanosilicate glass network. The characteristic timescale of this mechanism has been reported to be approximately 90 fs [31], which is comparable to the pulse duration used in this work. Therefore, this relaxation process is incorporated into the rate equation as a first-order decay term [30, 28]:

$$W_R = \frac{n(t)}{\tau_r} \quad (13)$$

where τ_r represents the average formation time of self-trapped excitons.

Finally, by substituting Eqs. (8), (10), and (13) into the rate Eq. (4), a nonlinear differential equation for $n(t)$ is obtained. Because of its coupled dependence on the time-dependent laser intensity $I(t)$ and the free-electron density $n(t)$, this equation generally has no closed-form analytical solution. Therefore, it is solved numerically using the fourth-order Runge-Kutta method. The numerical solution provides the temporal profile of the free-electron density, $n(t)$, for a laser pulse with specified parameters. This profile is then used in Eqs. (2) and (3), and the total absorption coefficient $\alpha_{tot}(t)$ is calculated based on Eq. (1). In this way, the proposed framework directly links the fs-IR laser parameters to the absorption-based threshold criterion, providing a practical basis for the controlled inscription and design of type I FBGs.

Table 1. Key material and laser parameters used in the simulations.

Parameter	Symbol	Value (Unit)
Core refractive index	n_{co}	1.45213
Cladding refractive index	n_{cl}	1.44692
Core bandgap	$E_{g_{co}}$	7.5 (ev)
Cladding bandgap	$E_{g_{cL}}$	9 (ev)
Exciton trapping time in core	τ_r	90 (fs)
Conduction band electron effective mass	m_e^*	0.65 of free electron mass
Laser wavelength	λ	1030 (nm)
Gaussian pulse shape	$I(t)$	$I(t) = I_0 \exp\left[-4\ln 2\left(\frac{t}{\tau_p}\right)^2\right]$
Pulse width, full width at half maximum of peak irradiance	τ_p	150 (fs)

https://doi.org/10.57647/pibm.2026.152601

3. Theoretical formulation for modeling the spectral response of type I FBG

To model the electromagnetic-field distribution in type I FBGs and investigate the effects of core–cladding mode coupling and realistic transverse RIM profiles on their spectral response, the vector Helmholtz equation for the electric field $\mathbf{E}(\mathbf{r})$ is solved in the three-dimensional grating geometry [32]:

$$\nabla \times (\frac{1}{\mu}\nabla \times \mathbf{E}) - k_0^2 \varepsilon_r \mathbf{E} = 0 \tag{14}$$

In this relation, $k_0 = \omega/c$ is the wave number in vacuum and the relative permittivity in a non-magnetic medium is defined as $\varepsilon_r = n_r^2$; where $n(r)$ represents the spatial profile of the refractive index.

In conventional FBGs, the RIM region is confined to the core, and the fiber cladding remains practically unchanged, maintaining a constant refractive index. In this work, to describe the spatial dependence of the refractive index in the fiber core, the refractive index profile is modeled as follows:

$$n_{\text{core}}(r) = n_0 + \Delta n \cdot g(x,y) \cdot f(z) \tag{15}$$

where n_0 denotes the base refractive index of the fiber core in the absence of the grating, Δn represents the amplitude of RIM induced by the inscription process, $g(x,y)$ describes the transverse RIM profile over the fiber-core cross section, and $f(z)$ characterizes the longitudinal RIM profile along the fiber axis.

In this analysis, the transverse function $g(x,y)$ is defined as shown in the schematic of Fig. 1 (b) to represent a profile with axial symmetry and radial inhomogeneity. According to this description, the RIM region is considered as a disk coaxial with the core and with diameter d, which does not necessarily cover the entire cross-sectional area of the core. Preserving axial symmetry suppresses coupling between modes with different azimuthal orders, allowing the analysis to focus on coupling among radially dependent core and cladding modes.

This choice is motivated by recent plane-by-plane FBG inscription methods [9, 33, 34], which can produce transversely structured RIM profiles that are more realistic than the ideal assumption of a uniform modulation over the entire core. Therefore, the proposed formulation provides a physically meaningful framework for analyzing type I FBGs inscribed using fs-IR lasers and enables a detailed investigation of how realistic transverse RIM profiles and core–cladding mode coupling shape the spectral response.

To evaluate the spectral response of the proposed structure, the vector Helmholtz wave equation (Eq. (14)) is solved in the frequency domain using the finite-element method (FEM) implemented in COMSOL Multiphysics. In this numerical model, the hybrid fundamental mode (HE_{11}) is launched into the structure through an input port, while perfectly matched layers (PMLs) are used to terminate the computational domain and suppress unwanted boundary reflections.

To ensure high numerical accuracy, the computational domain was discretized using a user-controlled mesh strategy. The maximum element size within the critical core and RIM regions was set to approximately $\lambda/8$, while a coarser mesh of about $\lambda/6$ was employed for the surrounding regions. This configuration resulted in a total of approximately 3.40×10^6 domain elements, characterized by an average element quality of 0.94 and a minimum quality of 0.50. Furthermore, the solver was configured with a relative tolerance of 0.01 to ensure stable convergence throughout the analysis. Finally, a frequency sweep corresponding to the selected wavelength range is performed, and the scattering parameters are obtained. The transmission and reflection spectra are then extracted as ($T = |S_{21}|^2$) and ($R = |S_{11}|^2$) respectively.

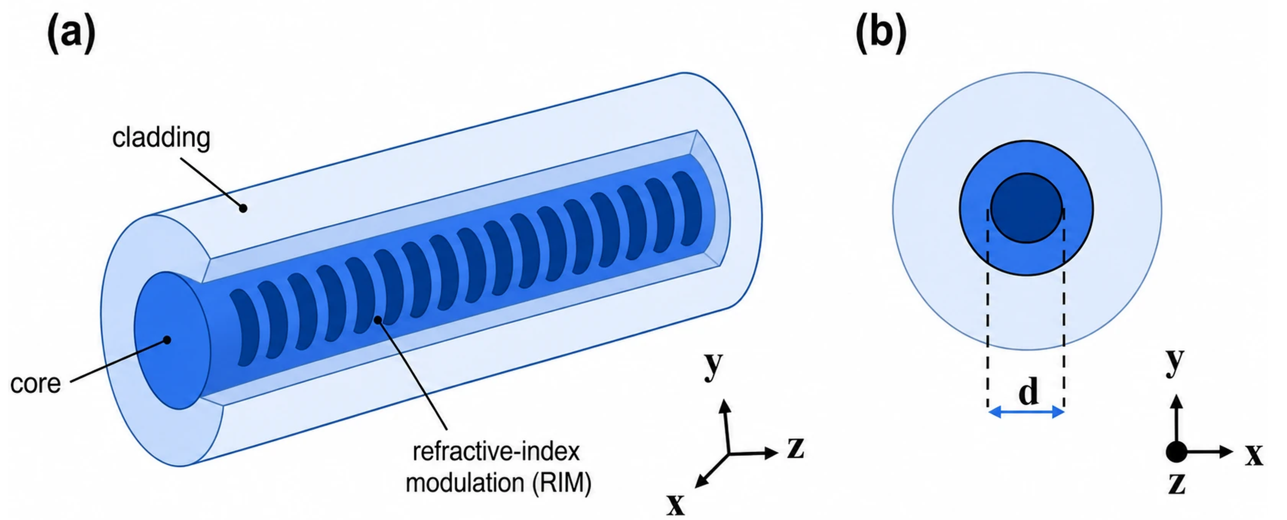

Figure 1. Schematic of FBG structure and RIM transverse profile. (a) General schematic of the FBG. (b) Cross-section of the fiber core with an axisymmetric and radially inhomogeneous profile, used to model the plane-by-plane fabrication method and to enable the isolated analysis of coupling to radially cladding modes.

https://doi.org/10.57647/pibm.2026.152601

4. Results and analysis

In this section, the modeling results and their analysis are presented in relation to the two main research challenges. In the first step, the single-pulse fluence threshold and peak intensity required for type I FBG inscription are determined, and the nonlinear processes governing this process are investigated. In the second step, the spectral response of these FBGs for RIM transverse profiles with axial symmetry and radial inhomogeneity is analyzed. All simulations are performed using realistic parameters corresponding to a standard SMF-28 single-mode fiber and a typical fs-IR laser inscription setup, the specifications of which are summarized in Table 1.

4.1 Threshold fluence and peak intensity for type I FBG inscription and the governing nonlinear mechanisms

In this section, the threshold peak intensity and fluence required to initiate type I FBG inscription are determined, and the nonlinear mechanisms associated with this threshold are analyzed. Using the theoretical framework introduced in section 2 and the parameters listed in Table 1, a Gaussian pulse with a peak intensity 1.3107×10^{13} W/cm^2 was used as the model input, and the temporal profiles of $\alpha_{tot}(t)$ and $n(t)$ were calculated. The corresponding results are presented in Fig. 2.

illustrates the direct connection between laser intensity, free-electron generation, and induced absorption. The nonlinearity of the material response is clearly evident in these results, such that $n(t)$ increases rapidly mainly in the time interval close to the pulse peak. This rapid increase in the free electron density directly leads to the growth of $\alpha_{tot}(t)$ and creates an almost simultaneous jump in the total induced absorption. Therefore, the results show that free-electron generation on a timescale of several tens of femtoseconds is the main mechanism responsible for laser-energy absorption during pulse irradiation. The absorbed energy is subsequently transferred to the glass network, providing the conditions required for type I RIM formation.

Figure 2 shows the temporal dynamics of $I(t)$, $n(t)$ and $\alpha_{tot}(t)$ for a representative pulse. Due to the strongly nonlinear and threshold-like behavior of the system, it is not very clear to compare several pulses with different peak intensities simply by overlapping the time plots, especially for the precise determination of threshold boundaries. Therefore, in order to achieve a clear comparison, the results are summarized numerically in Table 2. For this purpose, a set of pulses with different peak intensities was considered, keeping the wavelength (1030 nm) and pulse width (150 fs) constant, and for each pulse, the fluence and the maximum values of α_{tot} and n were extracted from the time profiles.

Analysis of the data in Table 2 shows that the system behavior is completely nonlinear with a distinct threshold point. At low intensities, for example, around 10^{12} W/cm^2, the absorption coefficient is very small and the amount of light absorption in the fiber is negligible, indicating no effective interaction. However, as the intensity increases to the order of 10^{13} W/cm^2, the maximum total absorption coefficient increases explosively by several orders of magnitude. This threshold behavior strongly strengthens the physical validity of our model, as it is in perfect agreement with numerous experimental observations showing that permanent changes in the refractive index during the interaction of fs-IR lasers with silica glass only begin at peak intensities above 10^{13} W/cm^2 [12, 13, 10, 11].

The central point of this analysis is the fourth row of Table 2, where the threshold condition is simultaneously satisfied in terms of peak intensity and fluence. In this case, the pulse peak intensity is 1.3107×10^{13} W/cm^2 and the maximum value of the absorption coefficient reaches 7.38×10^3 m^{-1}, which closely matches the experimental criterion $\alpha_{tot,exp}$. Accordingly, the fluence corresponding to this pulse, i.e. 2.092 J/cm^2, is identified as the threshold fluence for the onset of isotropic RIM formation and type I inscription. The close agreement of these values with the existing experimental reports under similar conditions [11, 24], not only confirms the validity of the presented model, but also shows that the proposed framework is able to determine the process threshold quantitatively and predictively.

Furthermore, the determined threshold intensity for SMF-28 fibers (1.3107×10^{13} W/cm^2) is consistent with values reported for other fiber types. For instance, in pure-silica core, the type I threshold has been observed in the range of $(1-2)\times10^{13}$ W/cm^2 [31], and in Yb^{3+}-doped aluminosilicate fibers, the threshold was determined to be approximately 1.21×10^{13} W/cm^2 based on nonlinear transmission measurements [35].

In addition to determining the threshold, Table 2 provides deeper physical insight. At the threshold fluence, the maximum free electron density is 1.69×10^{25} 1/m^3. This value is significantly lower than the critical plasma density (1.1×10^{27} 1/m^3 at 1030 nm [24]). This key observation confirms that type I inscription occurs in the dilute plasma regime and that the material has not yet undergone catastrophic optical breakdown.

In contrast, the last row of Table 2 illustrates the consequence of exceeding the type I inscription threshold. At a fluence of 2.235 J/cm^2 the free electron density reaches (3.25×10^{27} 1/m^3) exceeding the critical plasma density, while the total absorption coefficient rises to values above 10^6 1/m. This behavior indicates the onset of the structural damage regime and the transition toward type II inscription. Therefore, the present results identify not only the lower threshold for isotropic RIM formation, but also the upper boundary associated with damage initiation, thereby defining an optimal process window for the controlled and reproducible inscription of type I FBGs.

According to the results in Table 2 and the time dynamics shown in Fig. 2, it is clear that the reaching of α_{tot} to the threshold values is directly related to the rapid growth of the free electron population around the pulse peak. The next step is to identify the relative contribution of the electron production mechanisms in

https://doi.org/10.57647/pibm.2026.152601

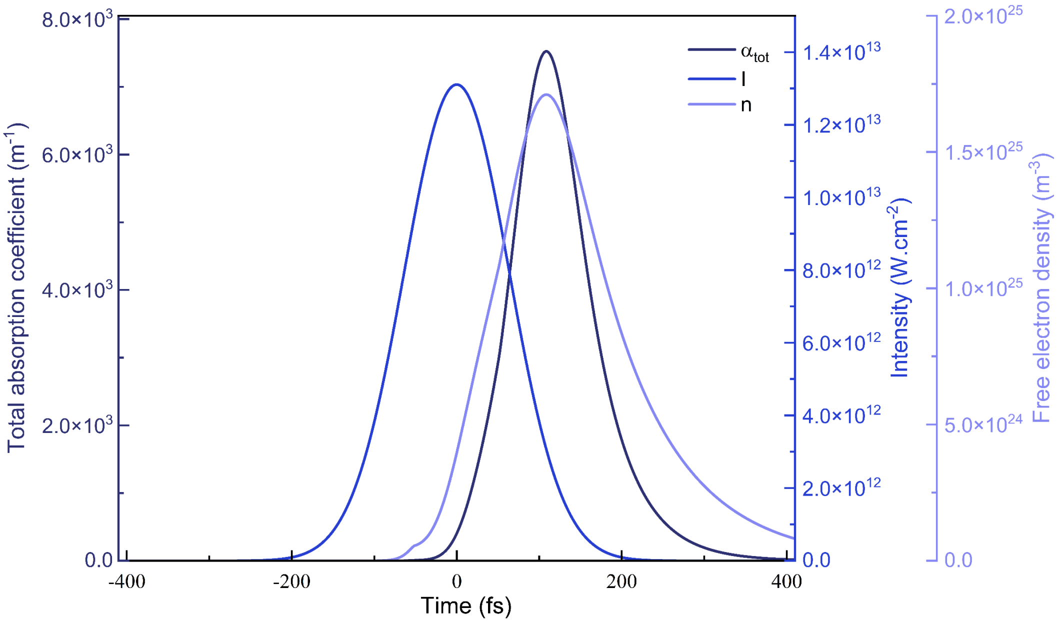

Figure 2. Simultaneous temporal evolution of the total absorption coefficient α_{tot}, free-electron density n, and instantaneous laser intensity I during the full duration of a femtosecond pulse (λ = 1030 nm, τ_p = 150 fs, $I_{Peak} = 1.3107 \times 10^{13}$ W/cm^2) in the fiber core. The horizontal axis is time (fs), with negative values indicating moments before the pulse peak. The left vertical axis shows α_{tot} in m^{-1}. The right vertical axes show I in W/cm^2 and n in m^{-3}.

this time interval. Therefore, to separate the role of the two main processes, the instantaneous multiphoton ionization rate $W_{\mathrm{MPI}}(t)$ and the avalanche ionization rate $W_{AV}(t)$ under the same pulse conditions (λ = 1030 nm, τ_p = 150 fs, and the peak intensity close to the RIM type I threshold) are calculated and displayed in Fig. 3 next to the intensity profile $I(t)$.

Direct comparison of these rates shows that, at the type I inscription threshold, multiphoton ionization clearly dominates seed-electron generation, whereas avalanche ionization exhibits a delayed onset and plays a secondary reinforcing role.

Beyond this threshold, however, the avalanche ionization rate increases sharply and eventually exceeds the multiphoton ionization rate. This behavior indicates that, at higher fluences, the system enters a strongly nonlinear regime in which cascade electron multiplication becomes dominant, promoting more severe structural modification and transition toward the damage-related type II regime.

Overall, this dynamic analysis indicates that the operational window for type I inscription lies in a regime where electron generation is primarily governed by multiphoton ionization and the free-electron density is sufficient to induce absorption, but remains below the level at which avalanche ionization dominates and structural damage begins. This mechanistic insight provides a basis for precise control and optimization of the type I FBG inscription process.

4.2 Modeling and analysis of the spectral response of type I FBGs with realistic transverse RIM profiles

The purpose of this section is to investigate the spectral response of type I FBGs by considering transverse RIM profiles and their effect on the predictability of the response in sensing applications. Before analyzing the spectral spectra, it is necessary to examine the electric-

Table 2. Maximum values of free electron density, total absorption coefficient, and laser pulse fluence at different peak intensities of the femtosecond laser (λ = 1030 nm, τ_p = 150 fs) to determine the fluence threshold required to create a type I FBG. The peak intensity values are chosen to include the region below and above the threshold.

Peak intensity (W/cm^2)	Maximum free electron density (1/m^3)	Maximum total absorption coefficient (1/m)	Pulse fluence (J/cm^2)
1×10^{12}	1.26×10^{18}	4.08×10^{-11}	0.169
1×10^{13}	1.69×10^{24}	73.62	1.44692
1.2×10^{13}	4.01×10^{24}	414.40	1.596
1.3107×10^{13}	1.69×10^{25}	7.38×10^{3}	1.916
1.32×10^{13}	2.62×10^{25}	2.62×10^{4}	2.092
1.4×10^{13}	3.25×10^{27}	1.53×10^{6}	2.107

https://doi.org/10.57647/pibm.2026.152601

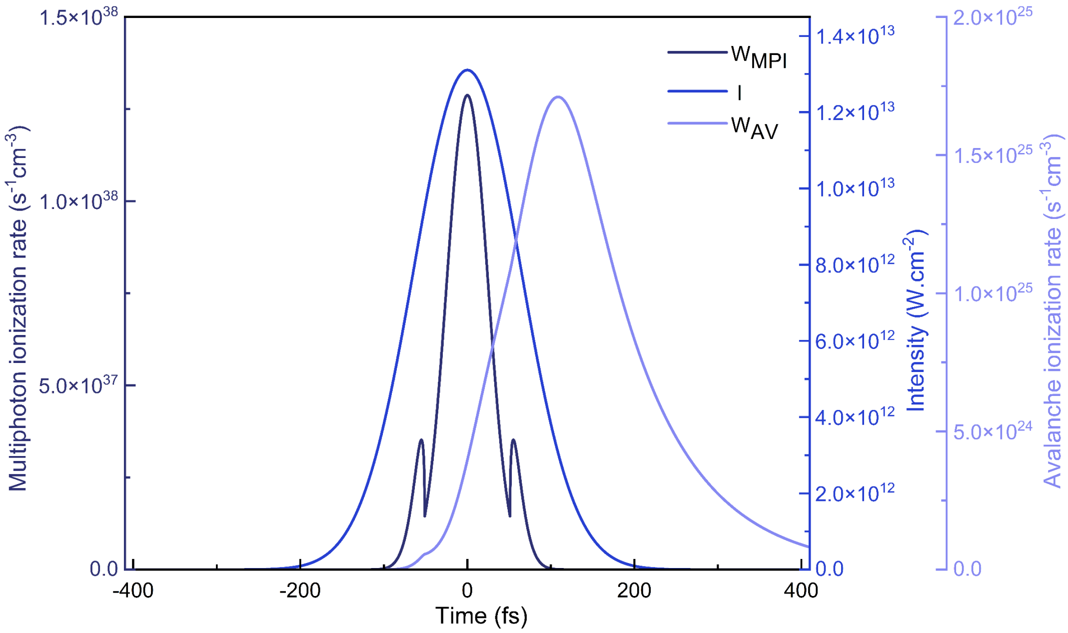

Figure 3. Temporal evolution of the multiphoton ionization rate, avalanche ionization rate, and laser pulse intensity in the fiber core over the entire duration of the femtosecond pulse (λ = 1030 nm, τ_p = 150 fs, I_{Peak} = 1.3107 × 10^{13} W/cm^2). The horizontal axis represents time in femtoseconds, where negative values correspond to moments prior to the pulse reaching its peak intensity. The left vertical axis indicates the photoionization rate in s^{-1} cm^{-3}, while the right vertical axes show the laser intensity in W/cm² and the avalanche ionization rate in s^{-1} cm^{-3}, respectively.

field amplitude distribution. This analysis provides both physical and numerical validation of the full-wave model, particularly in terms of port-mode excitation, boundary conditions, and mesh resolution. It also enables direct observation of power transfer from the core mode to cladding modes.

Accordingly, the electric-field amplitude distribution was simulated for a type I FBG inscribed in a standard SMF-28 fiber. The fiber has a core diameter of 8.2 µm and a cladding diameter of 125 µm. The simulated grating length is 1.5 mm, with a grating period of 534 nm. As an initial reference case for model validation, the RIM amplitude induced by the inscription process was set to $\Delta n = 10^{-3}$, and the RIM region was assumed to cover the entire core cross-section. The simulation results are shown in Fig. 4 for two wavelengths: one at the Bragg resonance (1549 nm) and one off resonance (1555 nm).

As shown in Fig. 4, field coupling from the core region to the cladding region and the excitation of cladding modes can be observed, indicating that these modes should not be neglected when modeling the spectral response of the FBG. At the off-resonance wavelength (Fig. 4 (a)), the electric field remains mainly confined to the core and propagates toward the fiber output, indicating dominant transmission and negligible reflection. In contrast, at the Bragg-resonance wavelength (Fig. 4 (b)), strong Bragg reflection and constructive interference produce a clear standing-wave pattern, and only a small fraction of the optical power reaches the output. This difference between the two wavelength cases demonstrates the function of the FBG as a wavelength-selective spectral filter, with strong reflection at the resonant wavelength and dominant transmission away from resonance.

The agreement between the simulated field distributions and the expected physical behavior of FBGs supports the correct implementation of the port definitions, boundary conditions, and full-wave numerical model. Based on this validation, the role of cladding modes and the effect of realistic transverse RIM profiles on the spectral response of type I FBGs can be investigated in the following analysis.

In the next step, to isolate the role of cladding modes and their coupling with the core mode, the transverse RIM profile is first assumed to be ideal and to fully cover the fiber-core cross-section. This reference assumption allows the intrinsic effect of core–cladding mode coupling on the spectral response of type I FBGs to be examined without the additional complexity introduced by transverse RIM inhomogeneity. Accordingly, Fig. 5 compares the transmission spectra of two simulated type I FBGs with identical parameters (L = 1.5 mm, Λ = 534 nm, $\Delta n = 10^{-3}$), In one case, coupling to cladding modes is included in the model, whereas in the other case this effect is intentionally neglected.

As shown in Fig. 5, when core–cladding mode coupling is not included, the transmission spectrum of the type I FBG exhibits a nearly symmetric Bragg resonance around the Bragg wavelength. This behavior indicates that the spectral response is mainly governed by coupling between the forward-propagating fundamental core mode and its backward Bragg-reflected counterpart, while additional coupling channels are suppressed in the model. In contrast, when core–cladding mode coupling is included, the overall spectral shape changes significantly. The Bragg resonance becomes asymmetric, and a series of side resonances appears at wavelengths shorter than the main Bragg resonance. These side resonances originate

https://doi.org/10.57647/pibm.2026.152601

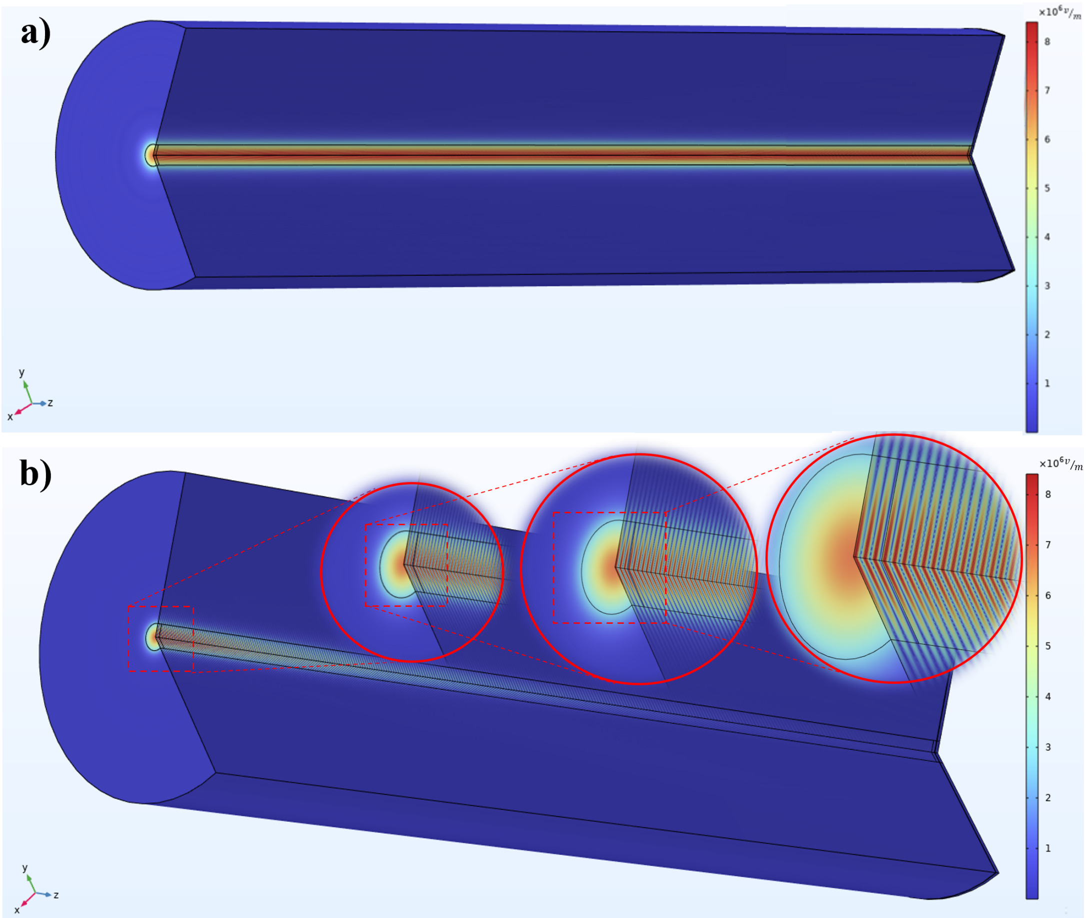

Figure 4. Electric field amplitude distribution in a type I FBG Inscription in SMF-28 fiber for (a) off-resonance wavelength and (b) Bragg resonance wavelength; enlarged views show details of the field interaction with the grating.

from the excitation of cladding modes and their coupling with the core mode, indicating that part of the optical power is transferred from the fundamental core mode to cladding modes and contributes to the overall spectral response.

Each of the narrow dips in the shorter-wavelength region relative to the Bragg peak originates from coupling between the core mode and a backward-propagating cladding mode. Since cladding modes exhibit a lower effective refractive index than the core mode, their corresponding resonances always appear at wavelengths shorter than the main Bragg resonance. The characteristics of these resonances, including their spectral spacing and strength, are governed by cladding-mode dispersion and the modal overlap integral, which directly determines the coupling coefficient. Furthermore as shown in Fig. 5, the presence of cladding modes not only induces side resonances, but also affects the main characteristics of the Bragg peak. Specifically, the Bragg wavelength undergoes a slight shift and the depth of the Bragg peak decreases, such that the minimum transmission increases. This decrease in depth is directly attributed to the leakage of some of the optical power from the core mode to the cladding modes, such that not all of the power is involved in the Bragg reflection process.

These results clearly show that neglecting cladding modes in modeling type I FBGs can lead to over-ideal predictions of the spectral response. In sensing applications, where subtle changes in the location and intensity of resonances carry physical or biological information, it is essential to consider these effects to achieve realistic and reliable predictions.

In addition to improving model realism, Fig. 5 provides a practical interpretation for sensing design: the core-dominated Bragg dip offers a stable reference feature, whereas selected side resonances are cladding-dominated and therefore substantially more sensitive to perturbations at the cladding boundary (e.g., changes in the surrounding refractive index or the formation of a thin biofunctional layer). Consequently, tracking one or more side resonances (wavelength shift and/or depth change) relative to the main Bragg dip enables differential interrogation strategies that can enhance robustness against common-mode effects such as temperature and axial strain.

To further assess the numerical robustness of the simulations, a mesh-independence study was performed. In addition to the standard computational grid, a finer mesh was constructed with an element size of approximately $\lambda/10$ inside the fiber core and $\lambda/8$ in the surrounding regions. The extracted Bragg wavelength was found to be 1552.95 nm for the finer mesh, compared to 1552.90

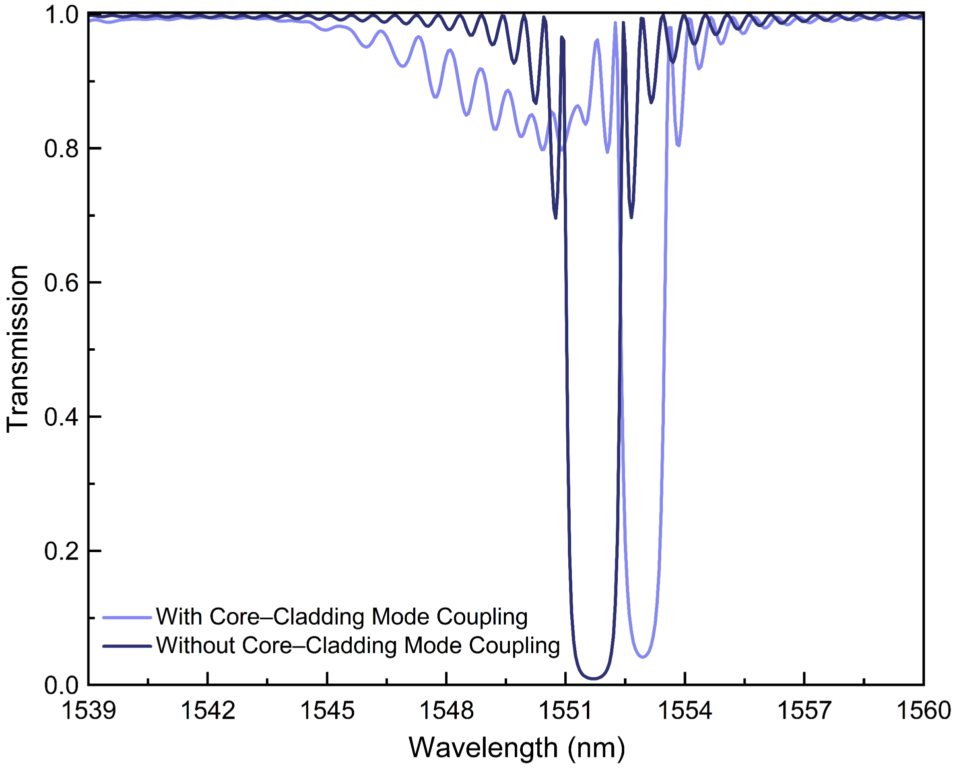

Figure 5. Simulated transmission spectra of two type I FBGs with identical parameters (L = 1 mm, Λ = 534 nm, Δn = 10^{-3}), comparing the cases with and without core–cladding mode coupling (see legend). Side resonances at wavelengths shorter than the Bragg dip indicate coupling to backward-propagating cladding modes

nm obtained using the standard mesh. The resulting difference of only 0.05 nm confirms that the reported spectral peak position and wavelength shifts exhibit negligible sensitivity to mesh refinement. These results demonstrate that the numerical predictions are robust and effectively independent of the discretization grid.

In the continuation of this analysis, the spectral response of type I FBGs was investigated by explicitly considering the coupling between the core mode and the cladding modes. In this framework, to evaluate the effect of the RIM region size on the intensity of the mode coupling and the resulting spectral characteristics, the defined transverse profile with different values of diameter d was simulated according to Fig. 1 (b) and the corresponding spectra were calculated and compared for each FBG. Figure 6 presents the simulated transmission spectra of four FBG structures sharing identical grating parameters (L = 1.5 mm, Λ = 534 nm, Δn = 10^{-3}), while differing solely in the cross-sectional area of the RIM region.

The results presented in Fig. 6 clearly demonstrate that the size of the refractive index modulation region plays a decisive role in shaping the spectral response of the FBG. As illustrated in the plot, increasing the diameter d enhances the overlap between the core mode field and the modulated region, thereby strengthening the Bragg reflection and reducing the transmission at the resonance wavelength. This behavior arises from the improved optical interaction between the core mode and the grating structure, which is directly governed by the dimensions of the RIM.

In addition, A closer analysis of the results in Fig. 6 shows that the dimensions of the RIM region, in addition to directly affecting the depth of the Bragg peak, play a key role in tuning the coupling strength between the core and cladding modes. In the case of complete core coverage, due to the high axial symmetry and uniform RIM distribution, the excitation of the cladding modes is limited and the spectral response takes on a more regular and symmetrical shape.

By reducing the diameter of the RIM to intermediate values, the refractive index discontinuity in the core cross-section becomes more pronounced and conditions are provided for more effective field scattering towards the cladding modes. This increase in core-cladding coupling leads to the transfer of part of the optical power from the fundamental mode to the cladding modes, which manifests itself in the form of a weakening of the Bragg peak and an enhancement of side resonances in the wavelength region shorter than the main peak. As a result, the transmission spectrum suffers from a pronounced asymmetry, which indicates the active participation of the cladding modes in the spectral response.

In contrast, by further reducing the RIM diameter to very small values, although the refractive index discontinuity still exists, the effective cross-section of the interaction between the optical field and the lattice structure is significantly reduced. In this case, a significant part of the optical field passes by the modulated region without strong interaction and the efficient coupling is

https://doi.org/10.57647/pibm.2026.152601

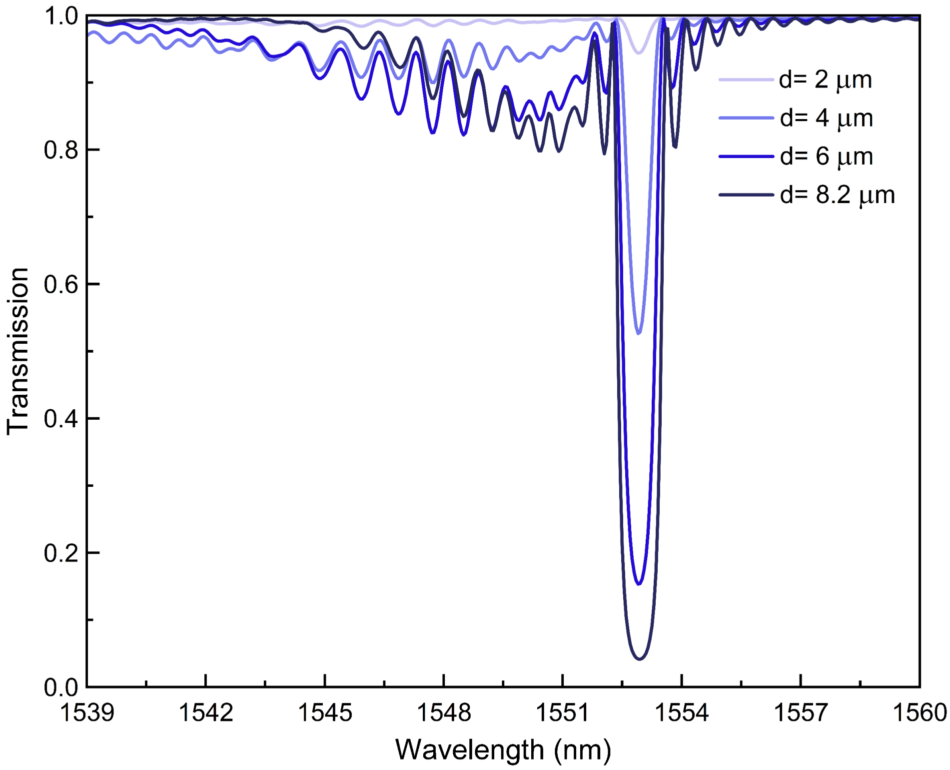

Figure 6. Simulated transmission spectra of type I FBGs with identical grating parameters (L = 1 mm, Λ = 534 nm, Δn = 10^{-3}) for different diameters d (2, 4, 6, 8.2 µm) of the transverse RIM region.

limited to the cladding modes. The consequence of this situation is the weakening of the side resonances and a partial restoration of spectral symmetry, although due to the overall reduction of the field overlap with the RIM region, the Bragg reflection is also reduced compared to the case of full core coverage.

The results of this section show that direct FBG inscription, by introducing a local discontinuity in the refractive index profile and breaking the transverse symmetry of the core, effectively increases the overlap integral between the core and cladding modes and enhances the coupling to these modes. This fundamental feature explains why many earlier models, which assumed a complete and uniform refractive index modulation confined to the core, failed to reproduce the pronounced side resonances appearing at wavelengths shorter than the main Bragg peak in experimental direct-inscription samples; such models inherently suppress core–cladding mode coupling and therefore do not predict the associated short-wavelength spectral features.

Furthermore, the present results demonstrate that side resonances loss is an intrinsic and non-negligible feature of directly inscribed type I FBGs and is not exclusively associated with type II gratings or structural damage. Even in type I FBGs with isotropic RIM and without material damage, the transverse morphology of the RIM, particularly the diameter of the modulated region d is sufficient by itself to induce pronounced attenuation and side resonances. In particular, variations in d not only regulate the strength of core–cladding coupling, but also modify the depth of the Bragg dip and the effective Bragg reflectivity, such that reduced field overlap with the RIM region leads to a weaker Bragg reflection and increased transmission at the resonant wavelength.

From a biosensing perspective, these findings are of particular importance, as both the Bragg wavelength position and the amplitude and shape of the Bragg resonance, as well as the side resonances associated with cladding modes, can carry sensing-relevant information and directly influence sensitivity, accuracy, and measurement repeatability. Accordingly, the full-vectorial model presented here, which simultaneously accounts for cladding modes and the realistic transverse morphology of the RIM region, enables not only the reproduction of near-real spectral responses but also their prediction and purposeful engineering. This framework provides a practical basis for the design of type I FBGs with controllable spectral characteristics tailored for advanced sensing and biomedical applications.

5. Conclusions

This study addresses two fundamental limitations that hinder the stable and reliable use of directly inscribed type I FBG in sensing systems, especially in biosensing and biomedical applications. In the first step, a physical framework based on rate equations is developed that allows for the quantitative determination of the inscription threshold with fs-IR by relating the nonlinear dynamics of electron production to a macroscopic experimental criterion. By simulating the laser irradiation conditions, this model characterizes the onset of isotropic and non-damaging RIM in the optical fiber and clearly delimits the safe operating window before the onset of structural damage. The results show that near the type I inscription threshold, multiphoton ionization is the dominant mechanism, while with increasing irradiation intensity and approaching the damage region, the contribution of avalanche ionization gradually increases and becomes the dominant mechanism.

In the second step, a full-wave and full-vector FEM-based model was presented that reproduces the spectral response close to reality, and considering the cladding modes. The results showed that the cladding modes not only cause lateral resonances in the region shorter than the Bragg peak, but can simultaneously break the spectral symmetry, reduce the depth of the Bragg peak, and even cause a measurable shift in the Bragg wavelength. More importantly, this study shows that the transverse morphology of the RIM and specifically the effective diameter of the modulated region is a decisive design parameter that tunes the Bragg reflection strength and the strength of the cladding core coupling. Accordingly, side resonances loss is not a phenomenon solely related to type II structural damage and can also occur intrinsically in type I, only due to the incomplete coverage of the core and local modulation.

To translate these results into a biosensing-oriented sensing strategy, the side-resonance set can be used as a sensitive interrogation channel because cladding-mode fields extend toward the cladding boundary and are directly perturbed by the surrounding medium. In a typical label-free assay, the fiber surface can be functionalized with capture probes, such as antibodies, aptamers, or ssDNA, so that binding of a target biomarker forms a thin adlayer and changes the local effective refractive index. In this configuration, the main Bragg resonance is expected to remain comparatively less sensitive to the external medium and can therefore serve as an internal reference.

Within our framework, controlling the transverse RIM profile - particularly the effective diameter d of the modulated region - provides a direct design knob to tune (i) the strength of core-to-cladding coupling, (ii) the number and contrast of accessible side resonances, and (iii) the trade-off between sensitivity and spectral simplicity. Stronger coupling (larger effective overlap with cladding modes) increases the interaction with the biointerface and can improve sensitivity, while weaker coupling yields fewer resonances and may improve selectivity and readout robustness by reducing spectral crowding. This establishes a practical route for engineering type I FBG spectra toward specific clinical targets, where different biomarkers can be addressed by selecting the most stable/high-slope resonance(s) or by using multiple resonances for multiplexed readout.

Authors contributions
All authors contributed equally to the conception, design, execution, and writing of this work. All authors read and approved the final manuscript.

Availability of data and materials
The datasets generated during and/or analyzed during the current study are available from the corresponding author on reasonable request.

Conflict of interests
The authors declare that they have no known competing financial interests or personal relationships that could have appeared to influence the work reported in this paper.

References

1. Jia D, Chao J, Li S, Zhang H, Yan Y, Liu T, and Sun Y. A fiber Bragg grating sensor for radial artery pulse waveform measurement. IEEE Trans Biomed Eng 2018; 65:839–46. DOI: 10.1109/TBME.2017.2722008
2. Haseda Y, Bonefacino J, Tam HY, Chino S, Koyama S, and Ishizawa H. Measurement of pulse wave signals and blood pressure by a plastic optical fiber FBG sensor. Sensors (Basel) 2019; 19. DOI: 10.3390/s19235088
3. Sun D, Guo T, Ran Y, Huang Y, and Guan BO. In-situ DNA hybridization detection with a reflective microfiber grating biosensor. Biosens Bioelectron 2014; 61:541–6. DOI: 10.1016/j.bios.2014.05.065
4. Loyez M, Lobry M, Wattiez R, and Caucheteur C. Optical Fiber Gratings Immunoassays. Sensors (Basel) 2019; 19. DOI: 10.3390/s19112595
5. Lo Presti D, Massaroni C, Jorge Leitao CS, De Fatima Domingues M, Sypabekova M, Barrera D, Floris I, Massari L, Oddo CM, Sales S, Iordachita II, TOSI D, and Schena E. Fiber Bragg Gratings for Medical Applications and Future Challenges: A Review. IEEE Access 2020; 8:156863–88. DOI: 10.1109/ACCESS.2020.3019138
6. Chen S, Zhang C, Wang J, Li N, Song Y, Wu H, and Liu Y. A Fiber Bragg Grating Sensor Based on Cladding Mode Resonance for Label-Free Biosensing. Biosensors (Basel) 2023; 13. DOI: 10.3390/bios13010097
7. Martinez A, Dubov M, Khrushchev I, and Bennion I. Direct writing of fibre Bragg gratings by femtosecond laser. Electronics Letters 2004; 40:1170–2. DOI: 10.1049/el:20046050
8. Zhou K, Dubov M, Mou C, Zhang L.and Mezentsev VK, and Bennion I. Line-by-line fiber Bragg grating made by femtosecond laser. IEEE Photonics Technology Letters 2010; 22:1190–2. DOI: 10.1109/LPT.2010.2050877

9. Roldan-Varona P, Pallares-Aldeiturriaga D, Rodriguez-Cobo L, and Lopez-Higuera JM. Slit beam shaping technique for femtosecond laser inscription of enhanced plane-by-plane FBGs. Journal of Lightwave Technology 2020; 38:4526–32. DOI: 10.1109/JLT.2020.2992568

10. Åslund ML, Jovanovic N, Groothoff N, Canning J, Marshall GD, Jackson SD, Fuerbach A, and Withford MJ. Optical loss mechanisms in femtosecond laser-written point-by-point fibre Bragg gratings. Optics Express 2008; 16:14248–54. DOI: 10.1364/OE.16.014248

11. Pallares-Aldeiturriaga D, Roldan-Varona P. RCL, and Lopez-Higuera JM. Optical Fiber Sensors by Direct Laser Processing: A Review. Sensors (Basel) 2020; 20. DOI: 10.3390/s20236971

12. Schaffer CB, Brodeur A, and MAZUR E. Laser-induced breakdown and damage in bulktransparent materials induced by tightly focused femtosecond laserpulses. Measurement Science and Technology 2001; 12:1784. DOI: 10.1088/0957-0233/12/11/305

13. Starke K, Ristau D, Welling H, Amotchkina TV, Trubetskov M, Tikhonravov AA, and Chirkin AS. Investigations in the nonlinear behavior of dielectrics by using ultrashort pulses (Best Oral Presentation). Laser-Induced Damage in Optical Materials 2004; 65:501–14. DOI: 10.1117/12.525132

14. Erdogan T. Fiber grating spectra. Journal of Lightwave Technology 2002; 15:1277–94. DOI: 10.1109/50.618322

15. Thomas J, Voigtlaender C, Becker RG, Richter D, Tuennermann A, and Nolte S. Femtosecond pulse written fiber gratings: a new avenue to integrated fiber technology. 2012; Wiley. DOI: 10.1002/lpor.201100033

16. Othonos A, Kalli K, Pureur D, and Mugnier A. Fibre bragg gratings. Wavelength Filters in Fibre Optics. 2006; Springer. DOI: 10.1007/3-540-31770-8_6

17. Khalid K, Zafrullah M, Bilal S, and Mirza M. Simulation and analysis of Gaussian apodized fiber Bragg grating strain sensor. Journal of Optical Technology 2012; 79:667–73. DOI: 10.1364/JOT.79.000667

18. Ikhlef A, Hedara R, and Chikh-Bled M. Uniform fiber Bragg grating modeling and simulation used matrix transfer method. International Journal of Computer Science Issues (IJCSI) 2012; 9:368

19. Mizunami T, Djambova TV, Niiho T, and Gupta S. Bragg gratings in multimode and few-mode optical fibers. Journal of Lightwave Technology 2000; 18:230–5. DOI: 10.1109/50.822797

20. Liu X, Wang Y, Li Z, Liu S, Wang Y, Fu C, Liao C, Bai Z, He J, Li Z, and Shao L. Low short-wavelength loss fiber Bragg gratings inscribed in a small-core fiber by femtosecond laser point-by-point technology. Opt Lett 2019; 44:5121–4. DOI: 10.1364/OL.44.005121

21. Thomas JU, Jovanovic N. BRG, Marshall GD, Withford MJ, Tunnermann A, Nolte, and Steel MJ. Cladding mode coupling in highly localized fiber Bragg gratings: modal properties and transmission spectra. Optics Express 2010; 19:325–41. DOI: 10.1364/OE.19.000325

22. Thomas JU, Jovanovic N, Kramer RG, Marshall GD, Withford MJ, Tunnermann A, Nolte S, and Steel MJ. Cladding mode coupling in highly localized fiber Bragg gratings II: complete vectorial analysis. Optics Express 2012; 20:21434–49. DOI: 10.1364/OE.20.021434

23. Couairon A, Sudrie L, Franco M, Prade B, and Mysyrowicz A. Filamentation and damage in fused silica induced by tightly focused femtosecond laser pulses. Phys. Rev. B 2005; 71:125435. DOI: 10.1103/PhysRevB.71.125435

24. Gaudfrin K, Lopez J, Mishchik K, Gemini L, Kling R, and Duchateau G. Fused silica ablation by double femtosecond laser pulses: influence of polarization state. Optics Express 2020; 28:15189–206. DOI: 10.1364/OE.387803

25. Wooten F. Optical properties of solids. 1972; Academic Press

26. Huang H, Kong F, Xia Z, Jin Y, Li L, Wang L, Chen J, Cui Y, and Shao J. Femtosecond-laser-induced damage initiation mechanism on metal multilayer dielectric gratings for pulse compression. Optical Materials 2018; 75:727–32. DOI: 10.1016/j.optmat.2017.11.030

27. Jing X, Shao J, Zhang J, Jin Y, He H, and Fan Z. Calculation of femtosecond pulse laser induced damage threshold for broadband antireflective microstructure arrays. Optics Express 2009; 17:24137–52. DOI: 10.1364/OE.17.024137

28. Gruzdev V. Fundamental mechanisms of laser damage of dielectric crystals by ultrashort pulse: ionization dynamics for the Keldysh model. Optical Engineering 2014; 53:122515–5. DOI: 10.1117/1.OE.53.12.122515

29. Keldysh LV. Ionization in the field of a strong electromagnetic wave. Zh. Eksperim. i Teor. Fiz. 1964; 47

30. Jupe M, Jensen L, Melninkaitis A, Sirutkaitis V, and Ristau D. Calculations and experimental demonstration of multi-photon absorption governing fs laser-induced damage in titania. Optics Express 2009; 17:12269–78. DOI: 10.1364/OE.17.012269

31. Lancry M, Poumellec B, Chahid-Erraji A, Beresna M, and Kazansky P. Dependence of the femtosecond laser refractive index change thresholds on the chemical composition of doped-silica glasses. Optical Materials Express 2011; 1:711–23. DOI: 10.1364/OME.1.000711

32. Feliziani M and Maradei F. Edge element analysis of complex configurations in presence of shields. IEEE Transactions on Magnetics 2002; 33:1548–51. DOI: 10.1109/20.582560

33. Wu J, Xu X, Liao C, Weng X, Liu L, Qu J, Wang Y, and He J. Optimized femtosecond laser direct-written fiber Bragg gratings with high reflectivity and low loss. Optics Express 2023; 31:3831–8. DOI: 10.1364/OE.482198

34. Li X, Chen F, Bao W, Wang R, and Qiaao X. Beam-shaping device-free femtosecond laser plane-by-plane inscription of high-quality FBGs. Optics & Laser Technology 2023; 161:109226. DOI: 10.1016/j.optlastec.2023.109226

35. Yunju Z, Zhongkai W, Yanan C, and Youyi Z. Multiphoton absorption and damage threshold of Yb^{3+} and Tm^{3+} doped SiO_2 fiber core. Academic International Symposium on Optoelectronics and Microelectronics Technology, IEEE 2011 :46–8. DOI: 10.1109/AISMOT.2011.6159312

36. Lancry M, Guizard S, and Poumellec B. Femtosecond laser direct writing in P, Ge doped silica glasses: time resolved plasma measurements. Femtosecond Laser Microfabrication 2009; Optica. DOI: 10.1364/LM.2009.LMTuA5